ANALYTICAL METHODS

X-RAY MICROTOMOGRAPHY

The X-ray tomography scans of the drill core samples were done with a custom-built Phoenix|x-ray Nanotom 180 NF (GE Measurement and Control) scanner at the University of Helsinki. The tungsten target X-ray tube was operated with an acceleration voltage of 135 kV and tube current 200 µA. The radiation was filtered with 0.5 mm of Cu. The samples were imaged over a full 360° circle with an angular step of 0.5° between projections. Each projection image was formed of an average of 10 exposures of 250 ms, with an effective pixel size of 31 µm. The projections were captured with a Hamamatsu flat panel sensor C7942SK-05. The 3D reconstructions were computed with datos|x – reconstruction software provided by Phoenix|x-ray.

X-RAY NANOTOMOGRAPHY

For the nanotomography scans, the arsenopyrite grains were mounted with cyanoacrylate glue to quartz glass capillaries (0.1 mm outside diameter, 0.01 mm wall thickness) which in turn were fixed to brass pins for mounting on the sample stage. The experiment was carried out on beamline ID16B (Martínez-Criado et al., 2016) of the European Synchrotron Radiation Facility (ESRF) with the experimental procedure known as holotomography (Cloetens et al., 1999). The experiment consisted of acquiring four tomographic propagation phase contrast datasets of each sample, while moving the sample between acquisitions to overcome the lack of information at certain spatial frequencies due to the Talbot effect. The transmission images of different sample-to-detector distances were then combined into a single map of the X-ray phase change for each projection angle in the phase retrieval step. This set of 2003 maps acquired over a 360° rotation was then tomographically reconstructed with the PyHST software. Both the phase retrieval code and PyHST have been developed at the ESRF. A quasi-monochromatic ("pink", $\Delta E/E \approx 10^{-2}$) beam of 29.6 keV X-ray energy was used for the imaging, and focused with multilayer Kirkpatrick-Baez mirrors to a 50 nm - 70 nm spot which was used as a secondary source. With this configuration, the magnification was partly geometric and the effective pixel size could be varied by changing the source – to – sample distance. Depending on sample dimensions, the voxel size of the reconstruction was 50 nm, 75 nm, 100 nm or 150 nm, corresponding

to the shortest source-to-sample distance (highest magnification) used in the scan. The source-to-detector distance was fixed at 705 mm. The images were recorded with a Frelon 4M camera (physical pixel size 24 µm), coupled to a scintillator screen with a 3.1 × magnifying eyepiece and 10 × magnifying optics. Exposure time per image was 1s. Each scan took approximately 4 hours.

TOMOGRAPHY DATA ANALYSIS

Ketcham (2005) has laid out 3-D quantitative mineral and fabric analysis using BLOB3D and QUANT3D, whereas Godel (2013) has applied the method to explore Ni-Cu-PGE deposits. In this contribution, the reconstructed volumes for both micro- and nanotomography were processed using Avizo (v.8.1 and 9.0, FEI, Hillsboro, OR, USA) to segment the volumes (i.e. divide the voxels into groups representing different minerals) and quantify the results, and Avizo and VGStudioMAX software (v. 2.1, Volume Graphics, Heidelberg, Germany) to visualize the results. Once the workflow was established, the analyses presented here took approximately one working day per sample for nanotomography, and approximately 5 hours per sample for the microtomography. Of course, this could be expected to decrease due to the operator gaining experience if a larger sample set is to be analysed by the same person. Prior to the analysis, the nanotomography data of individual arsenopyrite grains were treated with an in-house developed Matlab (Mathworks, Natick, Mass., USA) routine to correct for a gradient caused by X-ray intensity fluctuation during the scan. Most of the image processing operations used in the analysis are direct extensions of their 2-D-counterparts; for an overview to digital image processing and analysis, the reader is referred to an introductory text on digital image processing (e.g. Gonzalez and Woods, 2008).

Of the nanotomography data, a rough segmentation for visualization purposes could be achieved by successive dual threshold (hysteresis) binarization for each phase with different gray value (gold, arsenopyrite, pyrite, rutile), completed with the area selection (‘magic wand’) tool of Avizo. However, due to noise and artefacts in the image, this processing was not accurate in determining the boundaries of inclusions. Hysteresis thresholding could also not detect the smallest rutile inclusions, which due to the partial volume effect had a higher grayvalue than larger inclusions. Prior to quantitative analysis, a

more complex processing was performed to remedy these problems. For the nanotomography, this more accurate segmentation proceeded as follows:

1. The volumes were filtered using the Avizo implementation of the non-local means algorithm (Buades et al., 2005), done only in planes perpendicular to the long axis of the grain due to the long computation time.
2. The Canny edge detector algorithm (Canny, 1986) in Avizo was used to detect the boundaries between matrix and inclusions. The final edge image was the union of the Canny edges obtained by applying the algorithm in three orthogonal directions. The parameters of the edge detector were set very aggressively at this point, i.e. ensuring that all edges present in the image are retained, along with some spurious edges.
3. The edge image was morphologically dilated to ensure the continuity of the edges, and its inverse was labeled and used as seeds for watershed segmentation, with 3D gradient magnitude of the image used as the 'elevation' input. Based on visually investigating the data, the seeds with the smallest volume and/or lying closest to the crystal surface were filtered out of the data.
4. The resulting basins were assigned to different phases (exterior, rutile/pyrite, arsenopyrite, gold) based on the mean grayvalue within the basin, and obvious wrong assignments near the larger inclusions corrected manually.
5. The watershed lines were removed by successive dilation of each phase into the watershed lines.
6. Due to the large difference in x-ray attenuation and refraction between the arsenopyrite and surroundings (glue, capillary, air), the reconstruction exhibited some 'rippling' near the flat edges of the crystal, which caused some areas to erroneously be assigned to rutile/pyrite inclusions: these were manually re-assigned.
7. Finally, small inclusions with a barely noticeable grayvalue difference compared to the arsenopyrite were segmented by hysteresis thresholding a bottom-hat transform (the difference between an image closing and the original image) of the non-local means filtered data. To

avoid including the abovementioned ripples, only small inclusions further than 3 µm from the crystal surface were taken into account.

8. In the case of sample As101 also pyrite inclusions were observed in the crystal; these were separated from the rutile manually, based on their larger volume, higher grayvalue and euhedral shape.

In the case of microtomography, there are less artifacts in the image, but also the inclusions are smaller compared to the voxel size, which necessitates a different segmentation approach. Also in this case, partial volume effects and matrix texture caused some of the smallest sulfide grains to have insufficient contrast for a simple thresholding approach; the following process was used to separate the sulfides from the matrix and to divide them into two classes: euhedral, elongated arsenopyrite crystals and larger sulfide aggregates.

1. A top-hat transform (difference between the image and its opening) with a 5 x 5 x 5 voxel (155 x 155 x 155 µm) kernel was first applied to isolate the smaller diameter particles. Aggregates too big to be detected on the first pass were then found by applying a second top-hat transform with a 21 x 21 x 21 (651 x 651 x 651 µm) voxel kernel to the result of the first opening.
2. The results of both top-hat transforms were hysteresis thresholded to obtain an image with three phases: matrix, small diameter inclusions and large diameter inclusions.
3. To estimate the total particle count, touching particles were separated by taking the local maxima of both top-hat transformed images, and using these as seeds for watershed segmentation with the inverses of the top-hat transforms as elevation data.

In both cases (nano- and microtomography), the volume, surface area, orientation, and size along the long (X), intermediate (Y) and short axes (Z) of all objects larger than 10 voxels were determined with the particle analysis tool in Avizo. While the shape measurements for the very smallest of these objects can be inaccurate, this threshold selection will include practically all actual inclusions/sulfide grains, while eliminating noise-related clusters of only a few voxels from the results. The X-axis is defined as that along which the object has a maximum Feret diameter (distance between two parallel

planes touching but not intersecting the object), Z-axis as the one having the minimum Feret diameter and the Y-axis as the maximum Feret diameter perpendicular to the X-axis orientation. The Feret diameters for X and Z axes were sampled over 72 orientations over the half of the unit sphere, for Y-axis, 72 directions over a half circle are taken into account. It should be pointed out that with the discrete angular sampling and possibly concave shape of the object, the short axis is not necessarily perpendicular to the other two. An additional parameter used to describe the shape of the object is the shape factor, defined as:

$$Shape = \frac{Area^3}{36\pi \cdot Volume^2}.$$

The shape factor is therefore a dimensionless number, which equals 1 for a perfect sphere and increases as the shape becomes more irregular.

The advantage of this processing workflow in Avizo is that any single object in the results can be visualized and located within the volume, and the accuracy of segmentation and measurement verified vis-à-vis the original data. Based on such analysis, the shape factor was found to be a good indicator for segmentation success in the microtomography: objects with too low shape factor were mostly only fragments of a sulfide crystal, whereas those with exceedingly high shape factors were cases of failed separation of one or more touching crystals. For the orientation analysis of R473, only objects with shape factor between 1.8 and 4.5 were taken into account.

FIELD EMISSION-SCANNING ELECTRON MICROSCOPE (FE-SEM)

Electron optical analyses were performed at the Geological Survey of Finland using a JEOL JSM 7100F field emission scanning electron microscope attached to an Oxford Instruments EDS. The analytical conditions were as follows: high vacuum mode, a COMPO back-scattered signal (BSE), 20 kV accelerating voltage and 1 nA probe current.

REFERENCES NOT CITED IN THE ARTICLE

Buades, A., Coll, B., and Morel, J.M., 2005, A Non-local algorithm for image denoising: IEEE Computer Vision and Pattern Recognition, v. 2, p. 60-65.

Canny, J., A Computational Approach to Edge Detection: IEEE Transactions on Pattern Analysis and Machine Intelligence, v. 8, no. 6, p. 679-698.
Godel, B., 2013, High-resolution X-ray computed tomography and its application to ore deposits: from data acquisition to quantitative three-dimensional measurements with case studies from Ni-Cu-PGE deposits: Economic Geology, v. 108, p. 2005-2019.
Gonzalez, R.C. and Woods, R.E., 2008, Digital Image Processing, 3rd ed. Pearson Education Inc., New Jersey.
Ketcham, R. A., 2005, Three-dimensional grain fabric measurements using high-resolution X-ray computed tomography: Journal of Structural Geology, v. 27, p. 1217-1228.

FIGURE CAPTIONS

Figure DR1. Mineral quantification analyses of R473 and R477. A: Crystal volume vs. aspect ratio plot of arsenopyrite with mean aspect ratio around 3. B. Rose diagram showing random trends of the long axes of the arsenopyrite with respect to North, whereas the bottom plot shows the plunge angles. C: Flinn diagram showing the tendency of crystals towards elongate or rod-like shape. The X, Y and Z axes correspond to the maximum, intermediate and minimum Feret diameter in this and subsequent plots. D: Flinn plot of sample R477 showing roughly two-thirds of the aggregates (arsenopyrite and pyrite) inclined towards elongate or prolate shape. E: Crystal volume vs. aspect ratio plot with mean aspect ratio around 1.9. F. Rose diagram showing prominent peak of NNW-SSE correspond to the long axes (X) orientation of the aggregates. 3-D distribution of well-aligned sulfide aggregates superimposed on vertical and horizontal grayscale micro-CT slices.

Figure DR2. A: Arsenopyrite crystal is mounted with cyanoacrylate glue to glass capillary, which is fixed to a brass pin. B: Showing sample on the stage for nanotomography scan.

Figure DR3. Analyses of three arsenopyrite crystals (101, 102 and 104). A. Crystal volume vs. aspect ratio plot. B. Flinn plot clearly illustrates an elongate shape of the arsenopyrite crystals (cf. Fig. 3)

Figure DR4. Rutile analysis in arsenopyrite crystals 102 and 104. A: Crystal volume vs. aspect ratio plot of rutile inclusions within arsenopyrite 102. Mean aspect ratio is 2. B: Rose plot showing a preferred alignment of rutile long axes (X) orientations. C: Shape factor-volume plot, where volume gradually increases with the increase in the irregularity of rutile shape. D: Flinn plot showing equal distribution of oblate and prolate geometries. E: No relationship between the rutile aspect ratio and volume within the arsenopyrite crystal 104. Mean aspect ratio is 2.6. F. A preferred alignment of rutile long axes orientations. G: Shape factor-volume plot showing a similar pattern as observed in 102. H: Flinn diagram showing slight inclination of rutile grains towards oblate or disc-like geometry.

Figure DR5. A: Volume-aspect ratio of gold inclusions in arsenopyrite crystals (see Fig. 3), where volume increases with decrease in the aspect ratio. B: Flinn diagram showing a tendency of gold grains from sphericity towards prolate shape. C: Shape factor vs. volume plot showing increase in the irregularity of gold grains from close to sphericity with an increase in the volume. D: Pyrite volume-aspect ratio plot, where mean aspect ratio is around 1.7. E: Flinn plot of pyrite crystals showing most of the crystals are equidimensional.

Figure DR6.FE-SEM high-resolution textures of arsenopyrite from sample R473. A: Backscattered electron image (BEI) of arsenopyrite (crystal 21) showing gold (Au) grain associated with rutile. B: Ti elemental map of the same image shown in A. C: Distribution of gold in arsenopyrite (crystal 29). In each case gold is hosted by rutile. D, E: Ti and Au elemental maps of arsenopyrite shown in C. F: Arsenopyrite (crystal 34) showing gold grain inside rutile. G: Ti elemental map of the same arsenopyrite crystal 34.

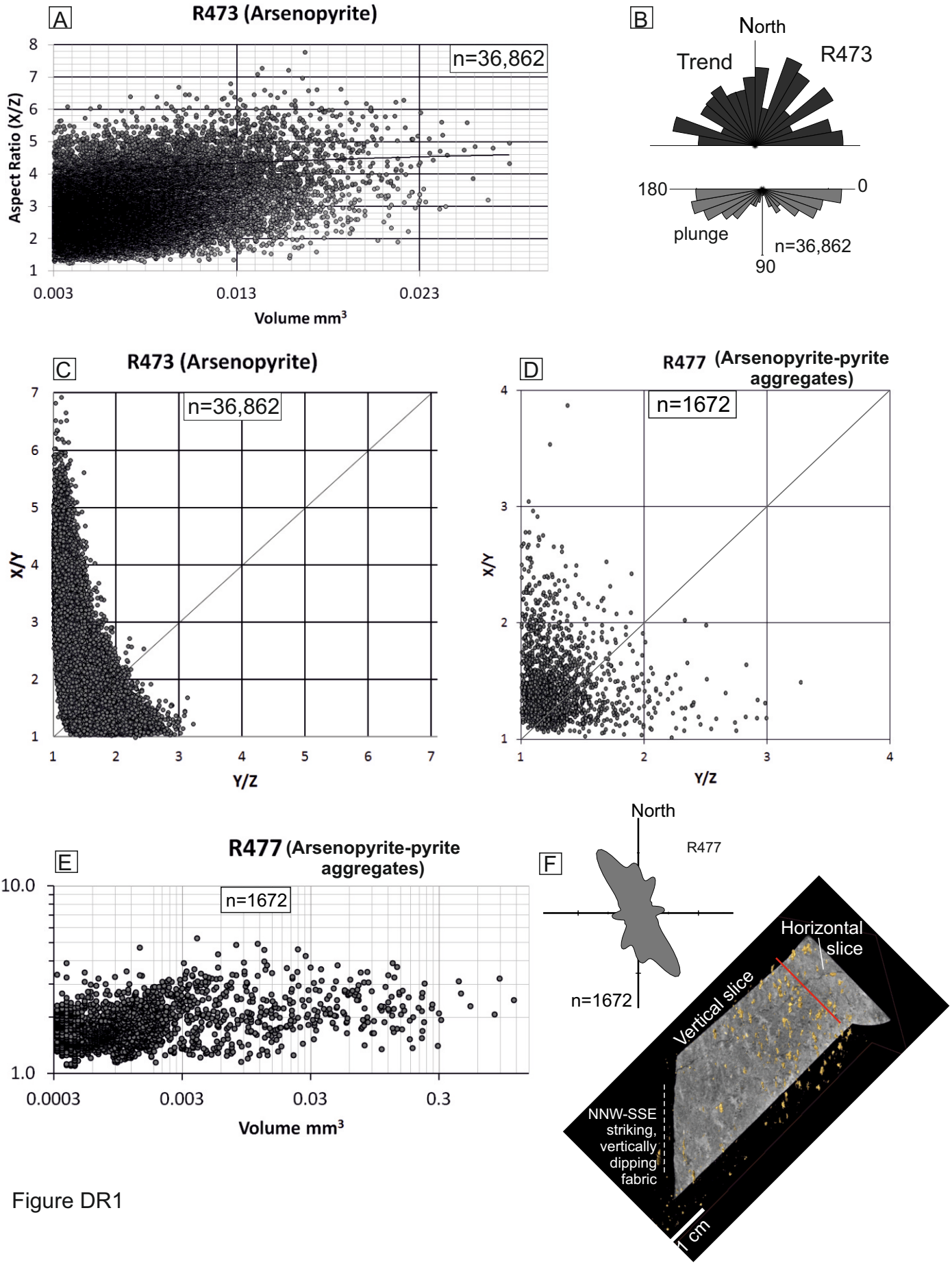
A
R473 (Arsenopyrite)
n=36,862
Aspect Ratio (X/Z)
Volume mm³
B
North
Trend
R473
180
0
plunge
n=36,862
90
C
R473 (Arsenopyrite)
n=36,862
X/Y
Y/Z
D
R477 (Arsenopyrite-pyrite aggregates)
n=1672
X/Y
Y/Z
E
R477 (Arsenopyrite-pyrite aggregates)
n=1672
Aspect Ratio (X/Z)
Volume mm³
F
North
R477
n=1672
Horizontal slice
Vertical slice
NNW-SSE striking, vertically dipping fabric
1 cm

Figure DR1

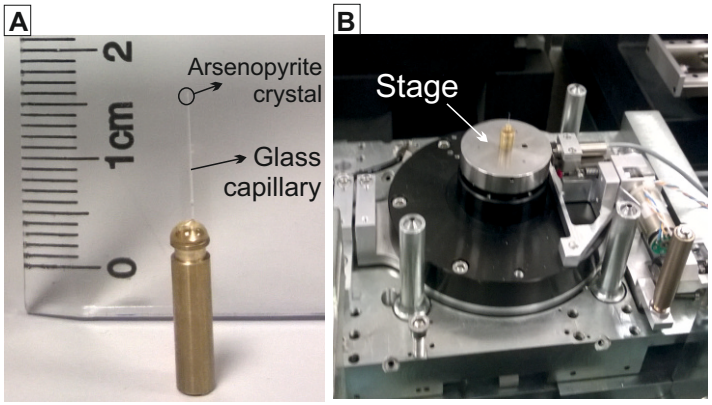

Figure DR2

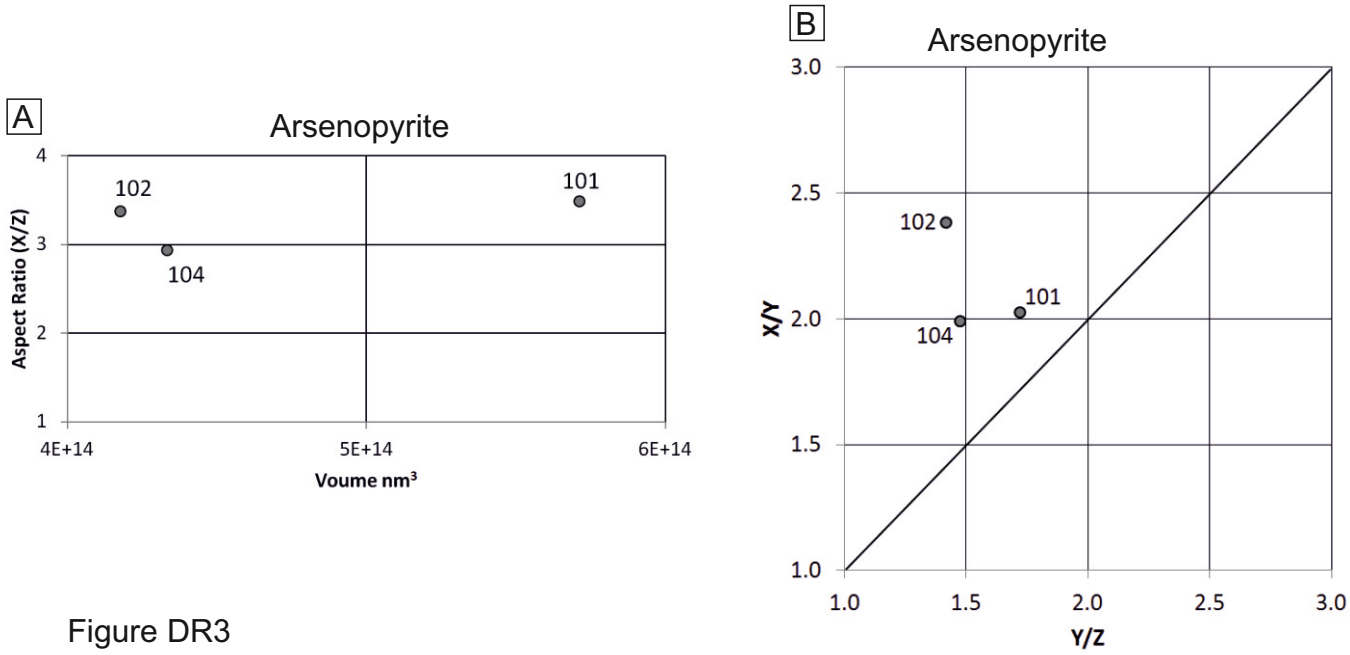
A
Arsenopyrite
Aspect Ratio (X/Z)
4
3
2
1
102
104
101
4E+14
5E+14
6E+14
Voume nm³
B
Arsenopyrite
X/Y
3.0
2.5
2.0
1.5
1.0
102
104
101
1.0
1.5
2.0
2.5
3.0
Y/Z

Figure DR3

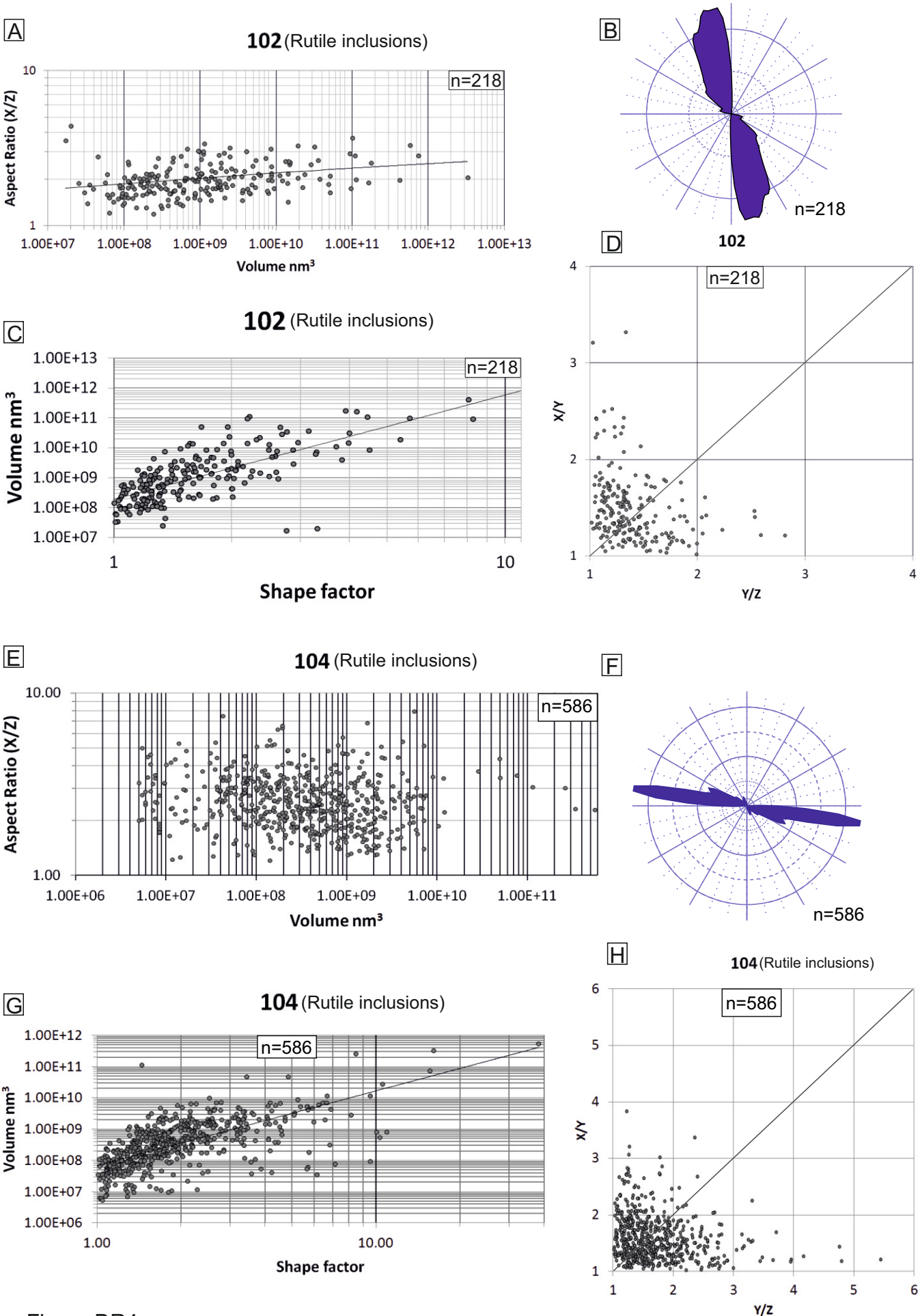
A
102 (Rutile inclusions)
n=218
Aspect Ratio (X/Z)
Volume nm³
B
n=218
102
C
102 (Rutile inclusions)
n=218
Volume nm³
Shape factor
D
n=218
X/Y
Y/Z
E
104 (Rutile inclusions)
n=586
Aspect Ratio (X/Z)
Volume nm³
F
n=586
G
104 (Rutile inclusions)
n=586
Volume nm³
Shape factor
H
104 (Rutile inclusions)
n=586
X/Y
Y/Z

Figure DR4

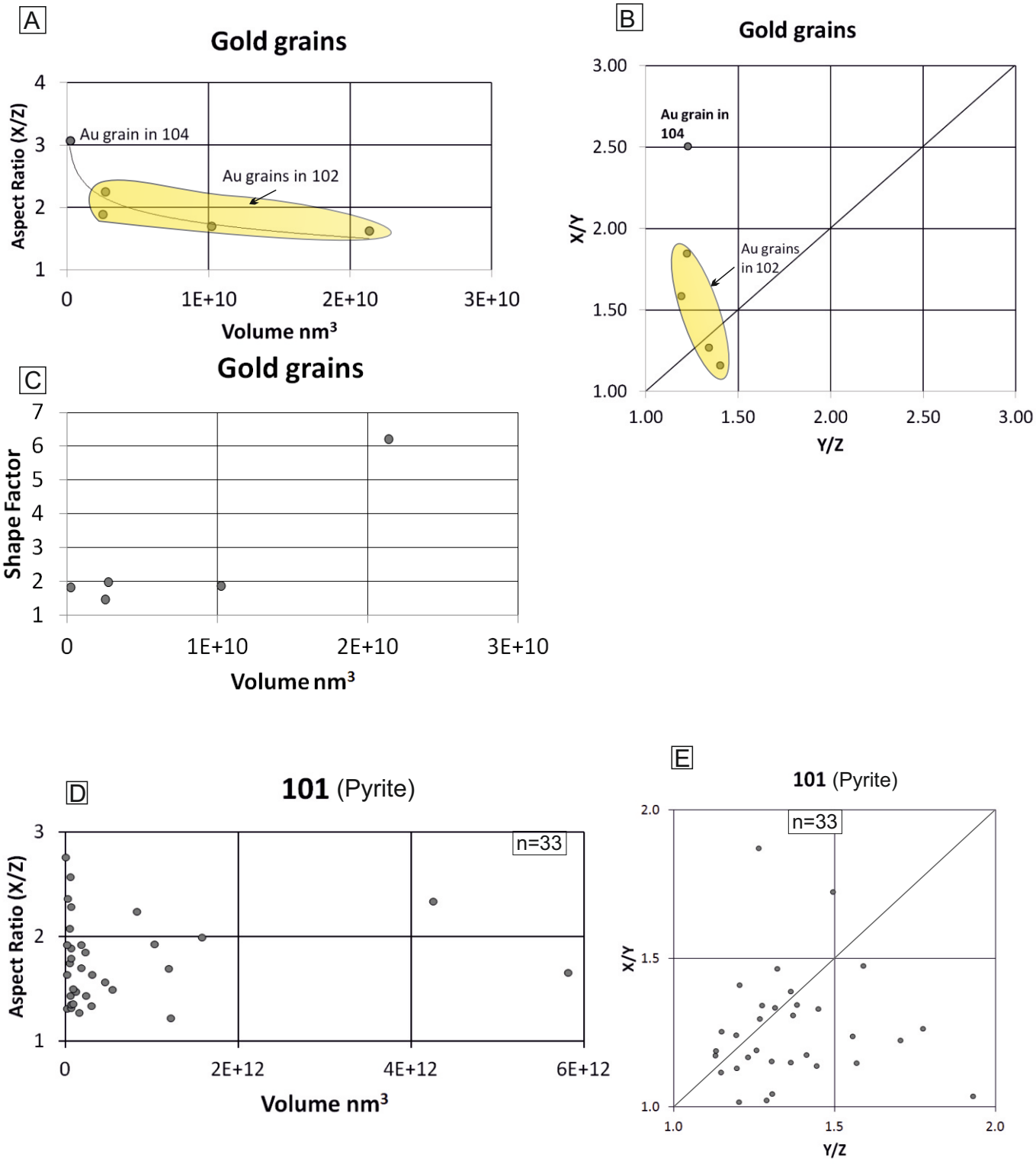
A
Gold grains
Aspect Ratio (X/Z)
Au grain in 104
Au grains in 102
Volume nm³
B
Gold grains
X/Y
Au grain in 104
Au grains in 102
Y/Z
C
Gold grains
Shape Factor
Volume nm³
D
101 (Pyrite)
n=33
Aspect Ratio (X/Z)
Volume nm³
E
101 (Pyrite)
n=33
X/Y
Y/Z

Figure DR5

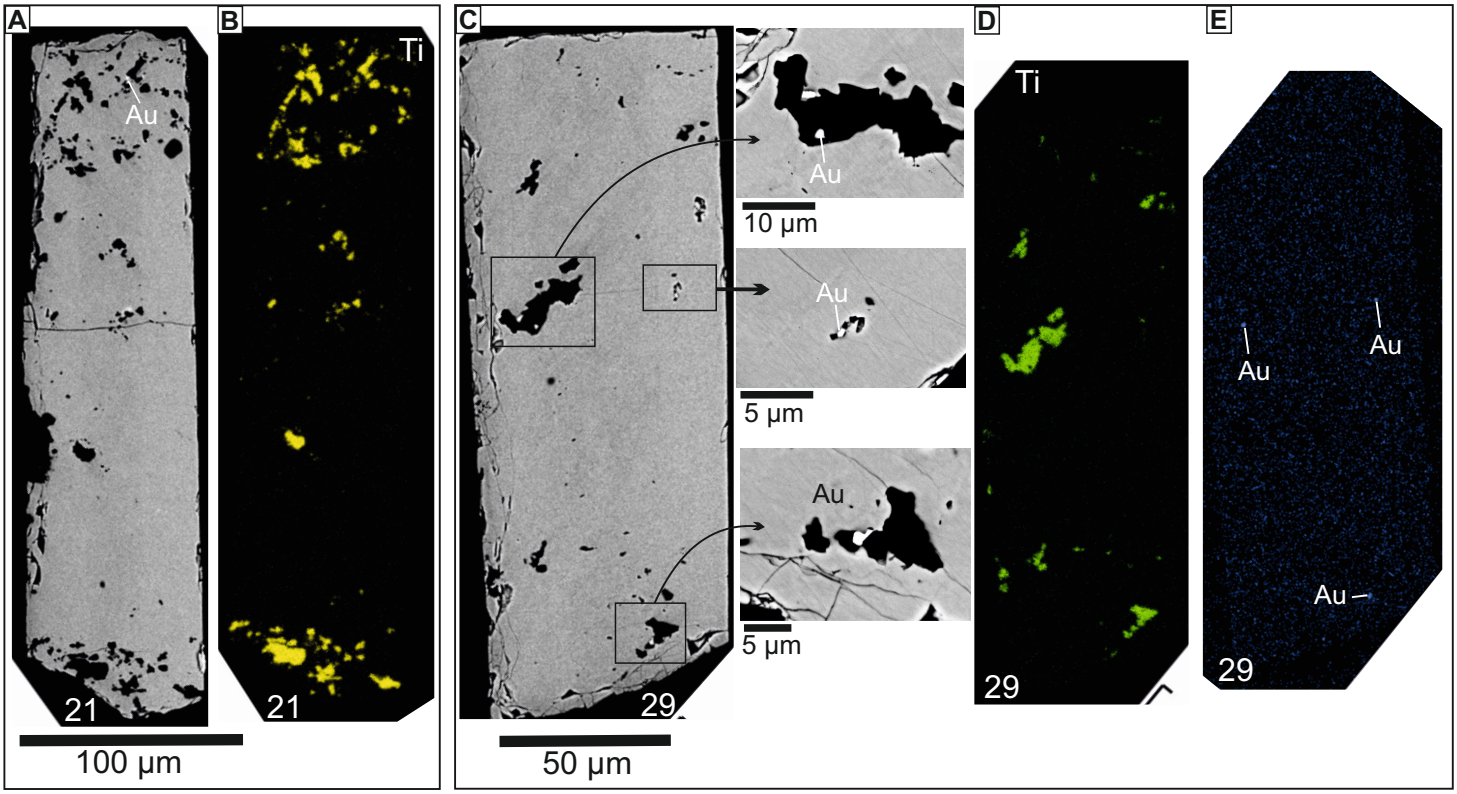
A
Au
21
B
Ti
21
100 µm
C
Au
10 µm
Au
5 µm
Au
5 µm
29
50 µm
D
Ti
29
E
Au
Au
Au
29

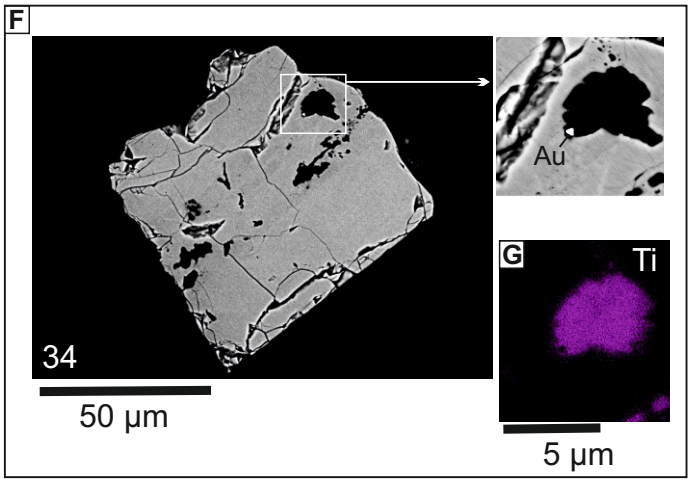
F
Au
34
50 µm
G
Ti
5 µm

Figure DR6